

Neural probe design for reduced tissue encapsulation in CNS

John P. Seymour, Daryl R. Kipke*

Department of Biomedical Engineering, University of Michigan, 2212 Lurie Biomedical Engineering Building, 1101 Beal Avenue, Ann Arbor, MI 48109-2099, USA

Received 3 November 2006; accepted 27 March 2007
Available online 5 April 2007

Abstract

This study investigated relationships between a microscale neural probe's size and shape and its chronic reactive tissue response. Parylene-based probes were microfabricated with a thick shank (48 μm by 68 μm) and an integrated thin lateral platform (5 μm by 100 μm , either solid or one of three lattice sizes). Devices were implanted in rat cerebral cortex for 4 weeks before immunostaining for neurons, astrocytes, microglia, fibronectin, laminin, and neurofilament. While nonneuronal density (NND) generally increased and neuronal density decreased within 75 μm of a probe interface compared to unimplanted control regions, there were significant differential tissue responses within 25 μm of the platform's lateral edge compared to the shank. The NND in this region of the lateral edge was less than one-third of the corresponding region of the shank (129% and 425% increase, respectively). Moreover, neuronal density around the platform lateral edge was about one-third higher than at the shank (0.70 and 0.52 relative to control, respectively). Also, microglia reactivity and extracellular protein deposition was reduced at the lateral edge. There were no significant differences among platform designs. These results suggest that neural probe geometry is an important parameter for reducing chronic tissue encapsulation.

© 2007 Elsevier Ltd. All rights reserved.

Keywords: Biosensor; Cell encapsulation; Foreign body response; Neural prosthesis

1. Introduction

Implantable chronic microelectrode arrays for neural recording are an important neurotechnology for systems neuroscience [1], with several emerging applications in neuroprosthetics [2,3]. While there are a number of studies reporting long-term recording properties of varied types of devices [4–9], central issues of recording stability, signal quality, and longevity remain. Reactive tissue response to the implanted device is considered to be a primary factor in the long-term performance of the devices. Probe treatments or designs that elicit reduced chronic tissue responses are of high interest.

Histological examination of intracortical devices has consistently shown that a glial sheath forms around the probe tract [10–12]. Cellular components of the glial sheath consist of activated microglia and hypertrophied astrocytes, and likely also include meningeal cells [13,14], and oligodendrocyte precursors [15]. These cell types produce

extracellular proteins that hinder local nerve regeneration [13,16]. In addition, a neuronal “kill zone” has been reported around neural probes [10,17]. After an injury, tissue encapsulation modifies the extracellular space as evidenced by mass transport [18] and impedance spectroscopy studies [9,19,20]. Injured CNS tissue loses volume fraction and gains tortuosity [21]. Tissue encapsulation is also concomitant with a decrease in the signal quality of neural recordings in the brain and the periphery [5,9,20,22–25]. These studies have motivated the pursuit of several approaches to reduce tissue encapsulation around implantable devices, including surface modification [26,27] and local drug delivery [28–30].

Modified microscale geometry may provide an alternative means of minimizing reactive cell responses. In vitro work has shown that macrophages do not adhere to or spread on polymer fibers ranging in diameter from 2 to 12 μm [31]. In vivo, single polymer fiber strands (diameters between 2.1 and 5.9 μm) in the rat subcutis have been shown to elicit decreased capsular thickness compared to larger diameter strands [32]. Additionally, substrate geometry and feature size has been associated with cellular

*Corresponding author. Tel.: +1 734 764 3716; fax: +1 734 786 0072.
E-mail address: dkipke@umich.edu (D.R. Kipke).

mechanotransduction in studies of adhesive substrate patterns looking at apoptosis and cellular spreading [33–35].

These studies helped to motivate our hypothesis that a subcellular-sized lateral edge will have less tissue encapsulation relative to the larger probe shank. To test this hypothesis, we implemented a probe design with a conventional, thick shank that supported a 5- μm -thick lateral platform. The thicker shank provided the structural strength to penetrate the rat pia matter and advance straight into the cortex. Furthermore, three of the four platforms were lattices of varying lattice width. The smallest lattice width was also hypothesized to induce less tissue encapsulation than the larger lattice width. The objective of this study was to investigate the relationship between probe size and shape and the reactive tissue responses in a chronic animal preparation. Whereas other studies have investigated differences of larger structures [12], we specifically considered probe elements on the subcellular level (5 μm). Encapsulation and neuronal loss were correlated with the different probe geometries by employing high-resolution confocal images to determine neuronal and nonneuronal cell densities. Double labeling with a variety of immunostains around the intact neural probe provided additional qualitative analysis of the device–tissue microenvironment, including astrocytes, microglia, and several extracellular matrix proteins.

2. Materials and methods

2.1. Neural probe design and fabrication

An SEM image and CAD layout of a lattice-like neural probe with subcellular features is shown in Fig. 1(a, b). This experiment tests four different platforms, one without a lattice and three with a lattice design of varying size (Fig. 1(b–e)). The specific dimensions chosen were greatly influenced by the size-dependent experiments discussed above. The shank dimensions were chosen to provide sufficient stiffness to penetrate the rat pia matter. To limit the number of variables, each design has identical outer dimensions and thus each design has an identical cross-sectional footprint. Each thin, lateral structure extends 100 μm and is 5 μm thick. Lattice size (4, 10, 30, and 100 μm , the last being solid) and the percentage of open area is unique to each. All of the probes had similar tip shapes (13°, chisel-shaped). Probe shank dimensions were measured to be $68.0 \pm 1.1 \mu\text{m}$ wide by $48.2 \pm 2.5 \mu\text{m}$ thick. The lattice width was 4.0 ± 0.2 , 9.8 ± 0.4 , and $29.5 \pm 0.5 \mu\text{m}$, respectively.

The probes were microfabricated in the Michigan Nanofabrication Facility. The fabrication did not include metallization. A sacrificial release layer of SiO_2 was grown on a 4-inch Si wafer (Fig. 2(a)). Parylene-C was deposited (5- μm thick) via chemical vapor deposition using a PDS-2010 obtained from Specialty Coating (Indianapolis, IN). A Ti layer 1000 Å was deposited and patterned for later use as a mask for the subcellular lattice structure (Fig. 2(b)). SU-8 2025 (Microchem, Newton, MA) was spin-coated to 38 μm ($\pm 2 \mu\text{m}$) and patterned to create the core of the probe shank (Fig. 2(c)). Oxygen plasma RIE surface treatment was applied before and after the SU-8 layer to improve interfacial adhesion. The second parylene layer was deposited 5- μm thick. This film conformed to the SU-8 backbone (Fig. 2(d)). We spun an 80- μm -thick AZ-9260 resist layer to cover the SU-8 structures and mask the shank of the probe (Fig. 2(e)). Parylene was etched using oxygen plasma RIE. Probes were released using hydrofluoric acid and then thoroughly rinsed in DI water, ethanol, and acetone (Fig. 2(f)).

2.2. Neural probe assembly

A stereotaxic frame was used to insert each probe with a controlled trajectory to minimize insertion damage and variability [17,36]. First a metal insertion plate (custom machined) placed on a glass slide is heated to $\sim 50^\circ\text{C}$, and then the glass slide was placed on a dissecting microscope. The probe head was mounted in the notched region of the heated insertion plate using poly(ethylene glycol) or PEG (8000 MW, Acros, Geel, Belgium). Rapid cooling prevented the PEG from wicking onto the shank of the probe.

The PEG and insertion plate were autoclaved separately prior to assembly. Probes were cleaned before and after assembly with 90% ethanol. Additionally, the probe and insertion plate assembly were sterilized with ethylene oxide (EtO) at ambient temperature and allowed to vent for 24 h under vacuum. When EtO sterilization was unavailable, ultraviolet exposure in a sterile hood for 30 min was used instead (two of seven animals). All probes in a given animal used an identical sterilization technique.

2.3. Surgical procedure

Multiple untethered probes were surgically implanted in male Sprague Dawley rats (300–350 g). Anesthesia was administered using intra-peritoneal injections of a mixture of ketamine, xylazine, and acepromazine. The craniotomy spanned approximately 4 mm in the anterior–posterior direction, and 3 mm in the medial–lateral direction and was centered over the M1 and M2 motor cortex. A $\sim 3\times$ stereoscope was used to ensure a nearly orthogonal trajectory and avoid any visible blood vessels. After a probe was inserted via a manual stereotaxic drive (coordinate range of 2.0–3.5 mm AP, 1.5–3.0 mm Lat), sterile artificial cerebral spinal fluid (Harvard Apparatus, Holliston, MA) was added to the craniotomy to release the probe from the insertion plate. By rotating the insertion plate and applying pressure to the probe head (height is 320- μm), the probe was then driven nearly flush with the brain surface to reduce transcranial tethering (Supplementary Fig. 1). Transcranial tethering would be expected to increase tissue reactivity [14]. Less than 200- μm of the probe was above the brain surface. Four probe types (Fig. 1(d–g)) were inserted in random order and orientation. One craniotomy contained all four neural probes, separated by a minimum of 0.5 mm. Surgical closure included a thin layer of purified calcium alginate followed by silicone and dental acrylic (Co-Oral-Ite Dental Mfg. Co., Diamond Springs, CA) [8]. All procedures strictly complied with the United States Department of Agriculture guidelines for the care and use of laboratory animals and were approved by the University of Michigan Animal Care and Use Committee.

2.4. Immunohistochemistry

Four weeks after implantation, animals were terminally anesthetized. Transcardial perfusion with 100 mL of chilled PBS was followed by 450 mL of 4% (w/v) paraformaldehyde in PBS. The brain tissue was removed and immediately explanted and post-fixed overnight in 4% paraformaldehyde. Following post-fixation, brain tissue was equilibrated in 30% sucrose in PBS and sectioned at 12 μm on a cryostat.

Tissue sections between cortical layers II and V were immunostained for each marker combination (see Tables 1 and 2) spanning approximately 1.1 mm of the cerebral cortex. The depth of interest was easily identified by the probe geometry seen in the transverse sections (see Fig. 1(b'–d')). Sections were not excluded or included based on the presence of a support arm. Sections were treated for 1 h with blocking solution at room temperature. All antibodies were diluted in blocking solution consisting of 4% (v/v) normal goat serum and 0.3% (v/v) Triton-X-100 for 6–10 h at room temperature. Alexa-488 and Alexa-568 labeled secondary antibodies (Invitrogen, Carlsbad, CA) were diluted in blocking solution to a concentration of 10 $\mu\text{g}/\text{mL}$. Secondary antibodies were incubated for 2 h at room temperature. All sections were counterstained with 2 $\mu\text{g}/\text{mL}$ Hoechst 33342 (Invitrogen) for 10 min. After washing with PBS, sections

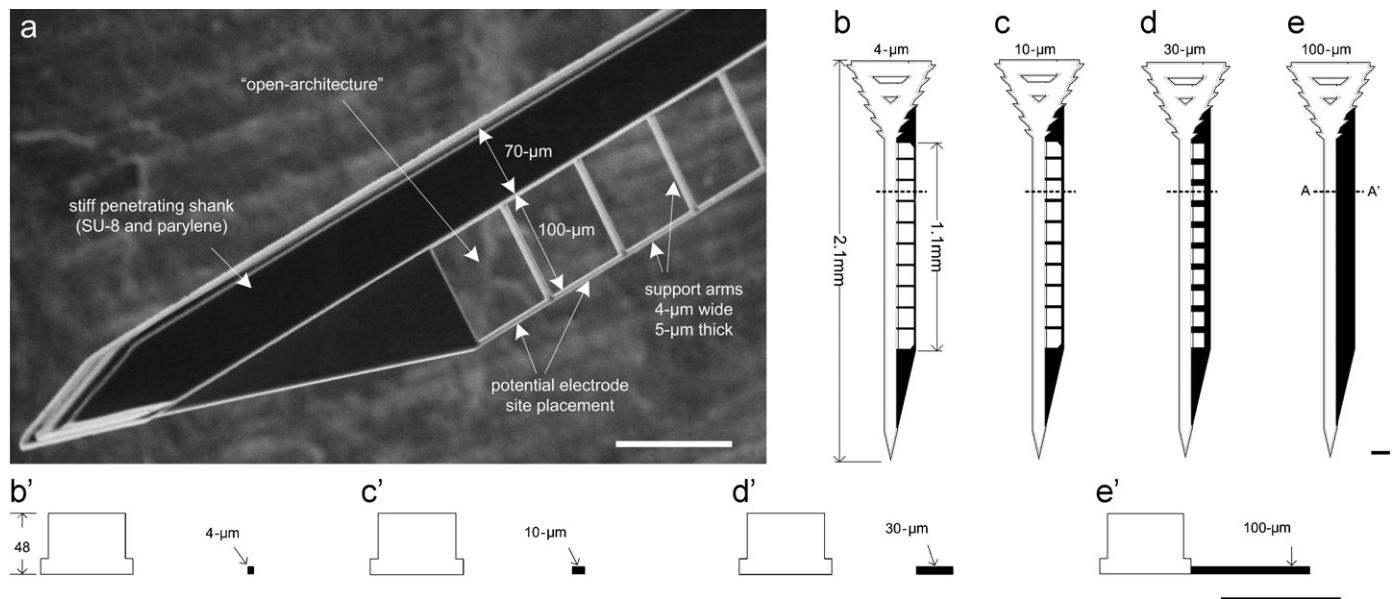


Fig. 1. Neural probe design with subcellular dimensions: (a) an SEM perspective view of a parylene-based open-architecture probe used for in vivo testing. The tip of the probe is at the lower left, (b–d) CAD drawings of each probe design indicating overall length and width of three lattice platforms (4, 10, 30 μm), and (e) one nonlattice platform (100 μm wide). (b'–e') Cross-sectional view of line A–A' shown in (b–e). All probes have identical shank and outer dimensions. Scale bars = 100 μm .

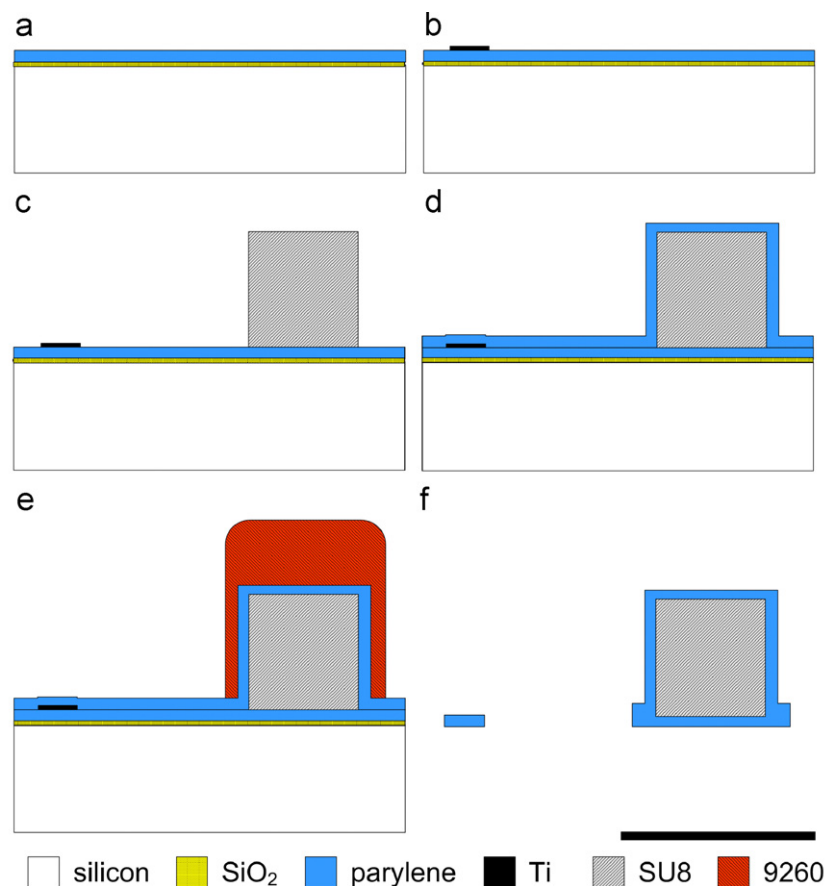


Fig. 2. Cross-sectional view of wafer level fabrication: (a) parylene deposited on SiO_2 sacrificial layer, (b) patterned titanium to mask parylene, (c) SU-8 patterned shank, (d) parylene encapsulated SU-8 structure, (e) 9260 resist patterned to form thick mask over shank, and (f) etched and released cross-section. Three masks used for photolithography in (b, c, e). X-scale = 100 μm (Y-scale approx.).

Table 1
Summary of antibodies

Antibody	Antigen	Cell type(s)	Isotype	Dilution	Vendor
GFAP	Glial fibrillary acidic protein	Astrocytes	IgG (rabbit)	1:400	Sigma
Fibronectin	Fibronectin	Fibroblasts	AI (rabbit)	1:800	Sigma
Laminin	Laminin	—	AI (rabbit)	1:400	Sigma
NeuN	Neuronal nuclei	Neurons	IgG1 (mouse)	1:1000	Chemicon
Neurofilaments	NF-M intermediate filaments	Neurons	NA (rabbit)	1:1000	Novus
OX-42	Neurons	Microglia, macrophages	IgG2a (mouse)	1:200	Serotec

AI-affinity isolated, NA = not applicable.

Table 2
Double label combinations

Double label	Number of animals	Minimum number of sections per animal
OX-42, GFAP	3	12
NeuN, GFAP	7	8
NeuN, laminin	7	8
OX-42, fibronectin	7	3
NeuN, neurofilament	3	4

Hoechst counterstain used with all.

were mounted with a coverglass using the antifade reagent Prolong Gold (Invitrogen).

2.5. Cell counting and statistical analysis

Eight transverse tissue sections spanning the length of the probe lattice structure (1.1 mm) were randomly chosen for cell counting. Confocal images were collected for these NeuN and Hoechst labeled sections using an Olympus FV500 (40 \times , oil immersion, NA = 1.3). A MatLAB graphical user interface was developed for off-line cell selection. First an outline of the intact probe or device–tissue interface was defined by a combination of a differential interference contrast (DIC) and UV fluorescence image (Fig. 3a). Small void spaces occasionally present between the probe and tissue as a result of tissue processing were included within the device–tissue interface boundary. A technician (blinded from study) selected all nuclei as either neuronal (NeuN+, Hoechst+) or nonneuronal (Hoechst+ only) from defined regions (lateral edge or probe shank). The technician was presented one optical slice at a time for each physical section, and four optical images per physical section (3 μ m step size spanning 9 μ m of tissue). Cells selected on the first optical image were clearly marked on the second image and so on until the fourth image was analyzed to prevent double counting (Fig. 3b shows the fourth optical section with the cumulative cell selection). Ultrathin optical sections (0.4 μ m) greatly improved the user's ability to uniquely identify cells. Two regions were bounded with a radius of 75- μ m from the device–tissue boundary (Fig. 3b). The probe shank region only included the three outside faces in order to avoid overlap with the lateral edge region. The lateral edge region also included the three outside faces, but only the first 5 μ m from the lateral-most point—regardless of the lattice feature size (4, 10, 30, 100 μ m). This rule ensured that all regions of interest were equidistant from one another.

After cell selection, the cell coordinates and device–tissue boundary coordinates were stored. A software algorithm used the center of each nucleus (user-selected) to calculate the shortest distance to the probe boundary, bin the counts by distance and region, and calculate the sampling area of each bin to form the processed data set.

Each count by bin and region (lateral edge or probe shank) was converted to density using area. Each density value was normalized by the mean contralateral density to produce unitless values. Contralateral tissue

images were identically processed using the cell selection user-interface and a generic device–tissue boundary overlay. Cells beneath the overlay were not counted.

A linear mixed effects model was used to evaluate the normalized responses of neuronal density, nonneuronal density (NND), and the ratio of the two. The fixed effects were the location (lateral edge or probe shank), the probe type (4-, 10-, 30- μ m lattice designs, and a 100- μ m solid design), and the interaction of location and probe type. The random effect in the model was the subject ($N = 7$). The model was fit by maximizing the restricted log-likelihood. Analysis was performed using the statistical package R 2.4.1 (www.r-project.org). Statistical significance was defined at the 5% level. We used a one-sided *t*-test to determine if cell densities around the probe types were different than the contralateral tissue, and whether an inherent bias existed in the contralateral control tissue (lateral edge or probe shank) (significance threshold of $p < 0.05$, $N = 7$ subjects).

3. Results

Seven male Sprague Dawley rats (300–350 g) were implanted with the four designs described above (Fig. 1(b, e)). There were no mechanical failures during insertion of these 28 probes. Dimpling rarely occurred during insertion. When dimpling did occur (possibly due to the presence of blood vessels near the pial surface [37]), the mild depression did not produce excessive bleeding. High-resolution images of the intact probes (transverse cryosections) revealed structural integrity out to 4-week post-implant (Fig. 3(a)).

The success of these surgeries and post-implant imagery showing structural preservation indicated that the tip angle, shank stiffness, and leading edge were sufficiently designed to pierce the rat neocortex in a straight trajectory and prevent damage to the fine 4- μ m \times 5- μ m \times 100- μ m parylene lattice. Larger lattice platforms also maintained their integrity.

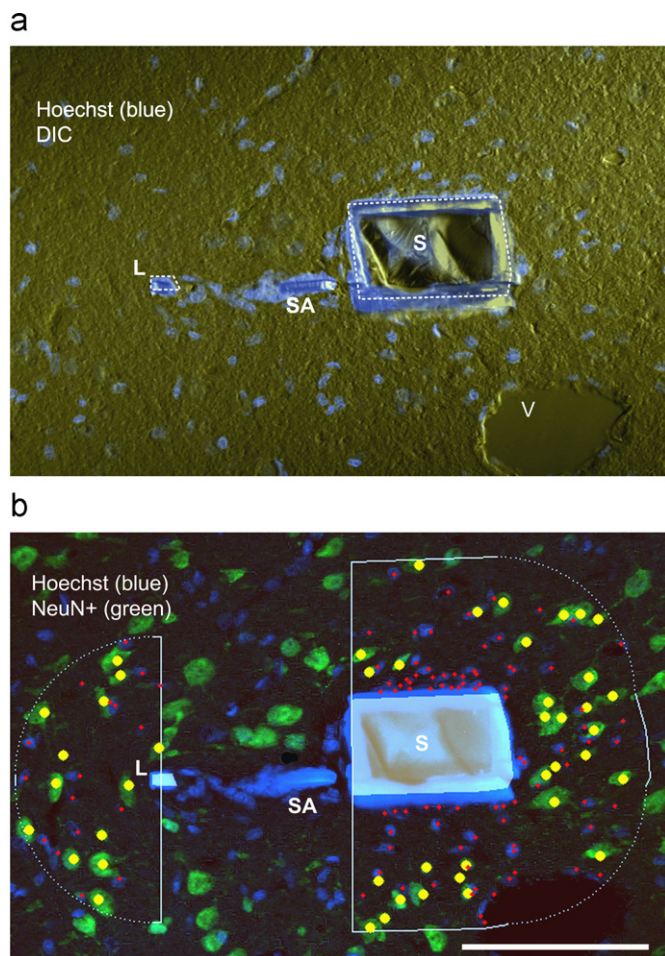


Fig. 3. Example images illustrating counting method. (a) Hoechst and differential interference contrast (DIC) image (4-μm probe) used to define the device-tissue interface, showing both lateral edge (L) and probe shank (S). This transverse section has a similar cross-section as shown in Fig. 1(b'). Portion of support arm (SA) was captured in section, as well as a large vessel (V). (b) Screen shot of technician-interface illustrating counting method. Red and yellow dots indicate selection of nonneuronal (Hoechst+, NeuN-) and neuronal cells (NeuN+), respectively. White borders are generated automatically and mark the 75-μm radius from the device-tissue boundary defined in (a). Left and right semi-circular regions represent the lateral edge (L) and probe shank (S) response regions. Scale = 100 μm. 40 × Obj.

3.1. Quantitative cell density as a function of probe geometry

Cellular encapsulation was hypothesized to be dependent on the size and shape of a given probe structure. In this context, we compare the cellular density by both lattice size (4-, 10-, 30-μm lattice structures, and 100-μm solid structure, all 5-μm thick) and the lateral edge (L) versus the probe shank (S).

3.1.1. Cell density in the contralateral hemisphere

Counting in the contralateral hemisphere of neuronal and nonneuronal cells defined the baseline for changes around the device-tissue interface. As expected, no

significant differences between the lateral edge and probe shank control regions existed for neuronal or nonneuronal cell density ($N = 7$ subjects).

3.1.2. Cellular encapsulation

A significant improvement in cellular response was found between the shank and lateral structure within the first 25 μm for all probe geometries. Fig. 4 provides four representative confocal images for each probe type. NeuN immunolabeling identified neurons and Hoechst counterstain identified nonneuronal cells (not NeuN+). A linear mixed effects model was used to evaluate the factors of probe type (4-, 10-, 30-μm lattice designs, and a 100-μm solid design) and location (lateral edge, probe shank) (Table 3). Only the location factor was significant. Beyond the 0–25 μm bin there was no significance for any factor. Interaction terms between the two factors was also tested but were not significant (data not shown).

NND for each probe geometry and distance bin was compared (Fig. 5). Encapsulation decreased dramatically around the shank beyond the 0–25 μm bin. When averaged across probe types (Fig. 5(b)) in the 0–25 μm bin, the NND was 2.29 ± 1.76 around the lateral edge compared to 5.25 ± 2.66 around the shank. This corresponds to an increase of 129% and 425% relative to contralateral tissue for the lateral edge and probe shank, respectively.

3.1.3. Neuronal density

Normalized neuronal density for each probe type and location was compared (Fig. 6). The location was the significant factor in predicting neuronal density ($p < 0.04$). Testing for significance between each platform type did not reveal a difference. Neuronal loss was greatest in the first distance bin where the immediate injury and secondary injury were expected to be foremost. When the normalized density was averaged for all probe types (Fig. 6(b)), the lateral edge value was 0.70 ± 0.33 and the probe shank was 0.58 ± 0.24 over the first 25 μm. This corresponds to a neuronal loss of 30% and 48%, respectively, relative to contralateral tissue.

3.2. Qualitative results: double label immunostaining

Several double labels were used to investigate the complex foreign body response around the probe. Table 2 lists the number of animals and minimum number of sections for each combination. GFAP (astrocytes), OX-42 (microglia), NeuN (neurons), fibronectin, laminin, and neurofilament immunostain combinations improve our understanding of the cellular and extracellular protein interactions in the central nervous system (CNS). A description and figure for the combination of laminin-/NeuN, and neurofilament-/NeuN is provided as supplemental information (Supplementary Figs. 2–3).

To illustrate variations between the responses at the lateral edge location and the shank, we provide two columns of images that were selected by the degree of

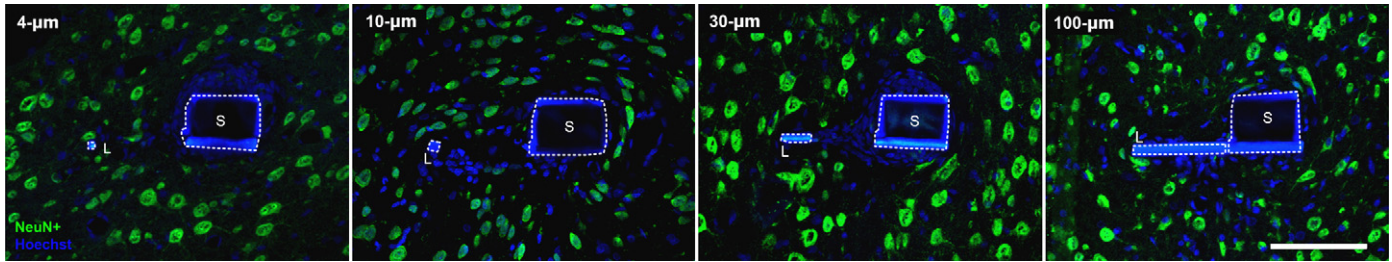


Fig. 4. IHC images showing NeuN+ reactivity (green) and Hoechst counterstain (blue) for each probe type. Probe type from left to right: 4, 10, 30, 100 μm . Parylene auto-fluorescence has greatest intensity in violet spectrum where the lateral edge (L) and shank (S) are easily identifiable. Scale = 100 μm . 40 \times Obj.

Table 3

Statistical factors influence cellular density (0–25 μm bin^a)

Response		Intercept ^b	10- μm lattice	30- μm lattice	100- μm solid	Probe shank
Neuronal	Coefficient ^c	0.78	−0.21	−0.06	−0.05	−0.25
Density	<i>p</i> value	NA	0.082	0.582	0.671	0.038
Nonneuronal	Coefficient	1.91	1.83	−0.25	−0.06	3.68
Density	<i>p</i> value	NA	0.054	0.791	0.950	0.0003

^aNo significance in factors beyond 0–25 μm bin.

^bModel intercept defined to be the lateral edge of the 4- μm lattice.

^cCoefficient values are relative to the intercept.

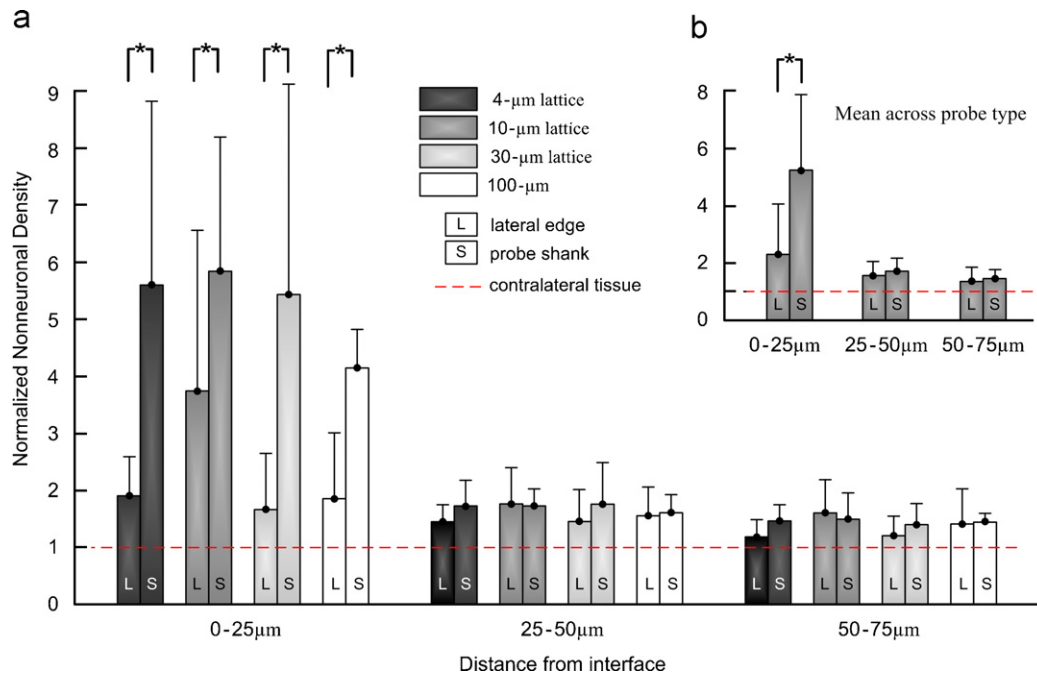


Fig. 5. Normalized nonneuronal density (NND) as a function of distance. (a) NND around each probe type and location. Density at the lateral edge (L) and probe shank (S) regions are paired together. In 0–5 μm bin, there was significance between lateral edge versus probe shank regions ($p = 0.0003$). (b) Mean NND for all probe types. Error bars denote standard deviation (S.D.). (Linear mixed-effects model, level < 0.05).

reactivity (Figs. 7–9). At the top of each column, the mean value of the NND is provided. The histological responses and descriptions are representative of two extreme cases in the dataset. Note that the contrast in reactivity between the columns of images is not intended to compare lattice width. The greatest variation in NND occurred around the probe

shank and not the lateral edge, where there were few examples of a high NND.

3.2.1. GFAP and OX-42

Two key cellular types in any CNS injury are astrocytes and microglia. GFAP+ tissue indicates astrocyte structure,

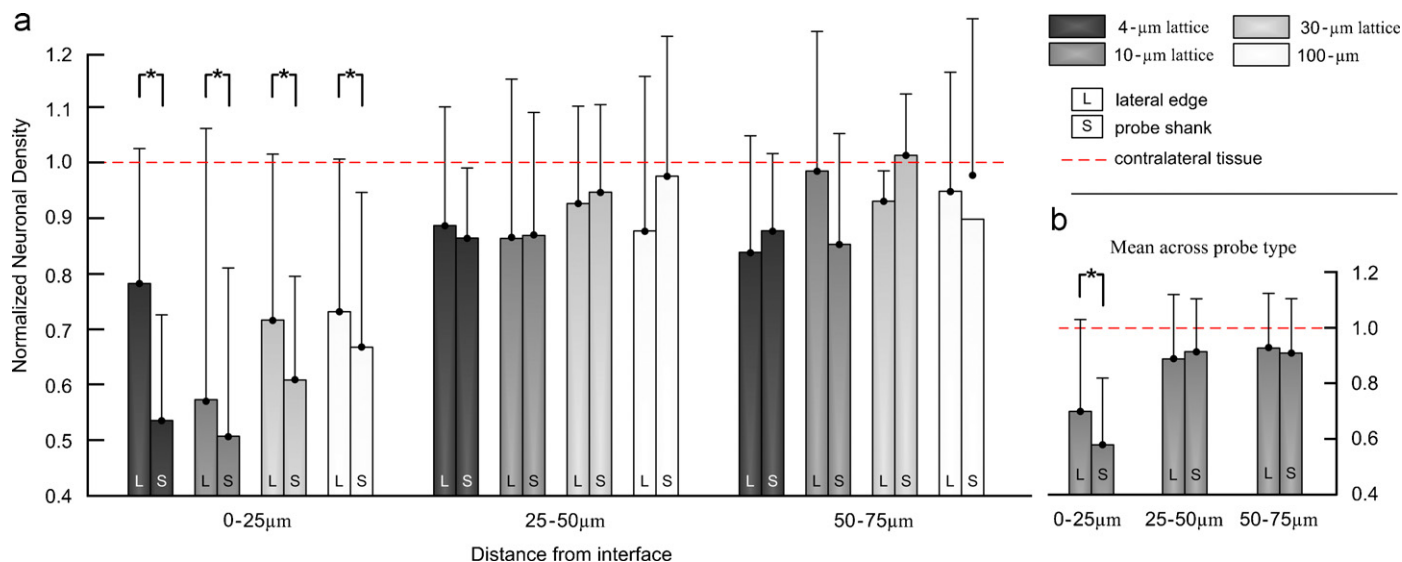


Fig. 6. Normalized neuronal density as a function of distance. (a) Neuronal density around each probe type and location. Density at the lateral edge (L) and probe shank (S) regions are paired together. In 0–5 μm bin, there was significance between lateral edge versus probe shank regions. (b) Mean neuronal density for all probe types. Error bars denote S.D. (Linear mixed-effects model, level <0.05).

and as seen in Fig. 7, a stellate, intertwined morphology forms around the device–tissue interface. In the low NND example on the left, GFAP reactivity was evident within several microns of both the lateral structure and shank, although less intense in the former. Around the high NND example (Fig. 7(d–f)), GFAP+ tissue circumscribed the probe shank and was approximately 10 μm distant from the shank. This demarcation between GFAP+ and densely packed nuclei (see Fig. 7(f)) was common wherever dense nuclei existed.

The OX-42 antigen is a CD11b integrin found on the surface of microglia and macrophages. Activated microglia exhibit an upregulation of CD11b and an amoeboid shape with few processes. Microglia exhibit finely branched structures with little cytoplasm when unactivated [38]. This study shows OX-42 reactivity was greatest at the interface, and the intensity and thickness of OX-42+ tissue corresponded well with dense capsular nuclei, consistent with previous studies [10,12,15]. OX-42+ tissue around a low NND interface was characterized by a mildly intense, thin layer, and concomitant with GFAP+ tissue (arrow in Fig. 7). When the cellular encapsulation layer was dense, the intense OX-42+ region that dominates the interface was devoid of GFAP+ reactivity (* in Fig. 7).

The morphology of OX-42+ structures at the lateral edge (Figs. 7 and 9) is important to note. Compact, amoeboid structures were rarely observed at the outside lateral edge; instead, finely branched processes were evident. While microglia were present around the lateral structure, qualitatively these cells did not exhibit the same morphology and compactness as those around the probe shank.

In summary, the regions around the far lateral edge had less encapsulation and OX-42 reactivity relative to the

shank. The morphology of OX-42+ structures also indicated a difference in phenotype between regions. GFAP+ tissue was always present at the lateral edge, but not always present immediately around the shank interface.

3.2.2. GFAP and NeuN

GFAP was present at the interface when cellular encapsulation was sparse (Fig. 8(a, e)) and displaced when the capsular cells were dense (Fig. 8(b, f)). Only occasionally was GFAP+ tissue observed deeply penetrating pockets of dense nuclei. NeuN+ structures were commonly found in and around intense GFAP+ tissue. Hypertrophied astrocyte-like processes were noted to extend around NeuN+ tissue when neurons were near the probe surface. This colocalization of astrocytes and neurons was expected [16]. In the two examples shown, neurons can be seen adjacent to the central lattice region and enveloped by GFAP+ filaments (* in Fig. 8). Incidences of neuronal survival within several microns of the lattice region occurred in only three of seven subjects.

3.2.3. Fibronectin and OX-42

Fibronectin labels meningeal fibroblasts in the CNS [13,39] and, like laminin, is a constituent of basal lamina. Fibronectin immunolabeling revealed a similar pattern of reactivity as observed with laminin (Supplementary Fig. 2). In low NND examples (Fig. 9(a, c, e)), fibronectin+ tissue was limited to the immediate probe interface and the inside corner of the probe (* in Fig. 9(a, c)). The high NND example (Fig. 9(b, d, f)) has a wider tract of tissue reactivity around the probe shank. OX-42 reactivity was also most intense at the interface but was not limited to the immediate probe interface. Interestingly, in many

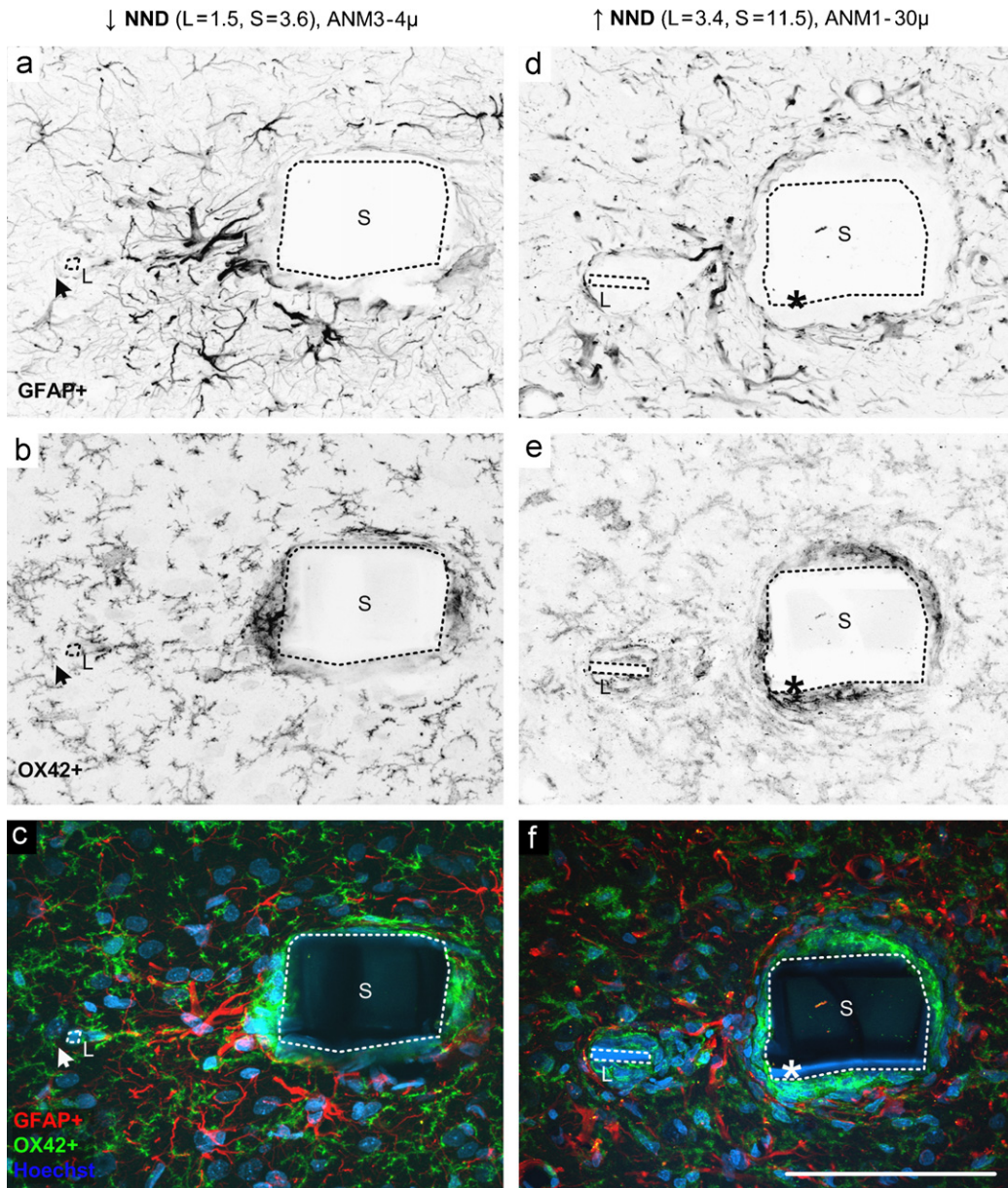


Fig. 7. Inverted grayscale IHC images (a, b, d, e) showing GFAP (a, d) and OX-42 reactivity (b, e), and the corresponding RGB color image including Hoechst (c, f). Mean value of nonneuronal density (NND) reported ($N = 8$ sections). (a–c) An example of a low NND. Tissue response around this type of interface was characterized by mild OX-42 reactivity, nearby ramified microglia, and OX-42 concomitant with GFAP+ tissue (e.g. arrow). (d–f) A high NND interface was characterized by intense OX-42 with an ameboid morphology, and a demarcation of GFAP reactivity (* in d–f). Scale = 100 μm . 60 \times Obj.

cases where encapsulation was pronounced, OX-42+ and fibronectin+ reactivity was similar in pattern but not always overlapping (arrows in Fig. 9). In many other images (data not shown), fibronectin and laminin was not present. Again, a difference in microglia phenotype was apparent in tissue around the shank versus the lateral edge.

3.3. Reactivity in the lattice region

The reactivity in the inside corner (nearest the shank) is often intense (Figs. 7–9), and sometimes even greater than

around the shank. In the middle of the lattice region, we see a variety of responses—from highly OX-42 and fibronectin reactive to the other extreme of GFAP and NeuN reactive. The presence of neurons was only occasionally seen and not necessarily “inside” the probe lattice. In general, the encapsulation and OX-42 reactivity of the lattice region was similar to that found around the shank of the probe, and with no apparent dependence on lattice size (data not quantified).

An example confocal image showing a support arm segment succinctly captures a pattern found around the three regions of interest—probe shank, lattice region, and

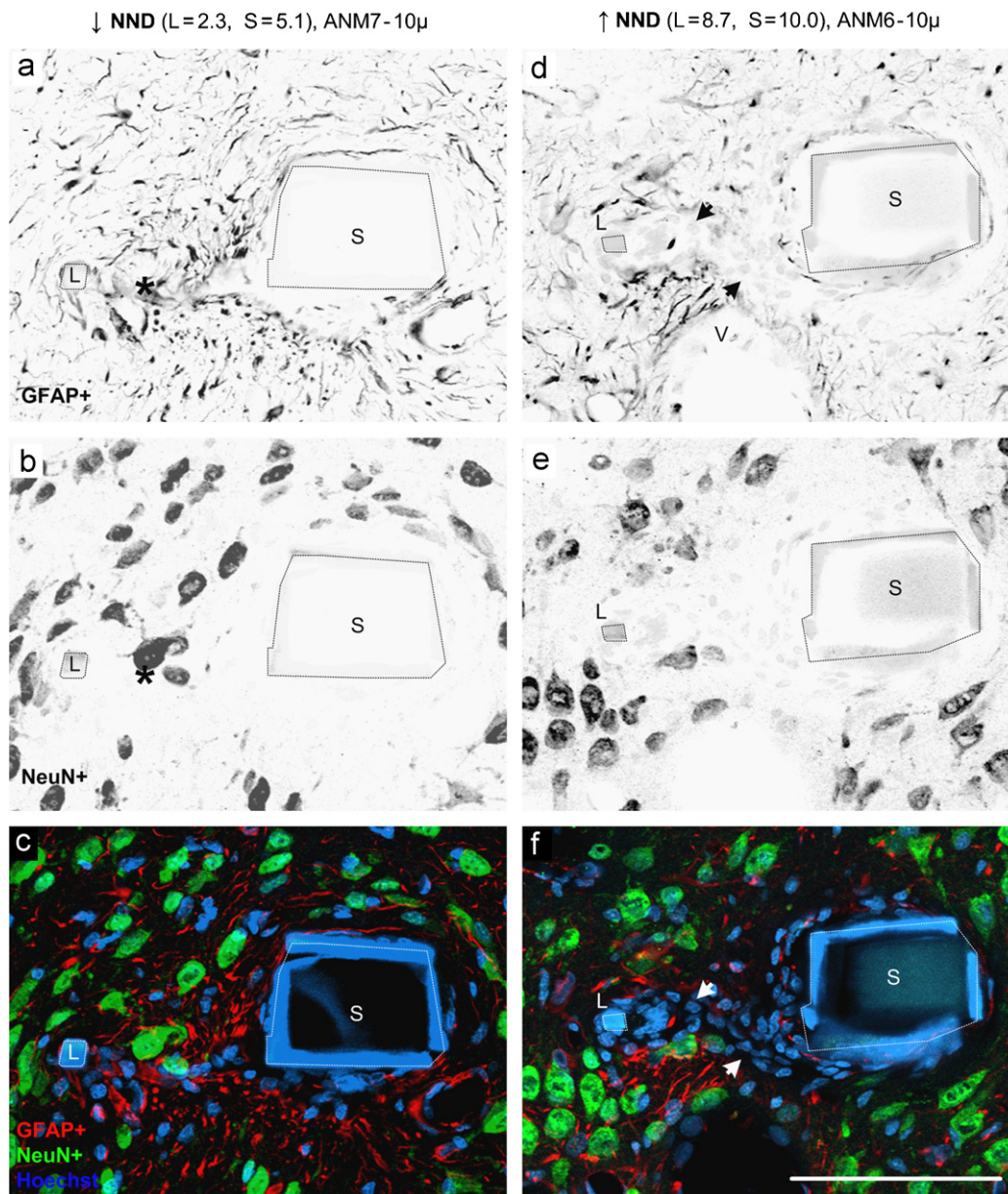


Fig. 8. Inverted grayscale IHC images (a, b, d, e) showing GFAP (a, d) and NeuN reactivity (b, e), and the colocalization of these including Hoechst counterstain in RGB color (c, f). (a–c) A low NND was characterized by a concurrence of NeuN+ and GFAP+ tissue (* in a, b). (d–f) Few neurons were near the high NND interface. In these cases, GFAP- and dense encapsulating cells characterized the probe interface and open-architecture region (arrows, d, f). Scale = 100 μm. 60 × Obj.

platform lateral edge (Fig. 10). The first layer of parylene around the shank has been rotated 90° due to cryosectioning or processing and effectively provides a coronal view of nuclei adhering to its surface (see arrows). The nuclei were disc-shaped and relatively large. Around the support arm, three-dimension confocal images (not shown) revealed the nuclei to be elongated in one dimension—along the length of the support arm. The morphology of nuclei at the outside lateral edge were relatively small, spherical, and sparsely packed. These nuclei were rarely elongated or conformal to the edge despite this structure having identical dimensions as the support arm. Additionally,

intense but narrow laminin+ tissue (Supplementary Fig. 2) was outlining the shank and support arm structures, but not the outside edge.

4. Discussion

The contrast in encapsulation and neuronal loss between the shank and lateral edge described above demonstrates a differential chronic tissue response between the probe shank and the platform's lateral edge. The degree of neuronal loss reported here is smaller than two other quantitative reports on the biocompatibility of neural

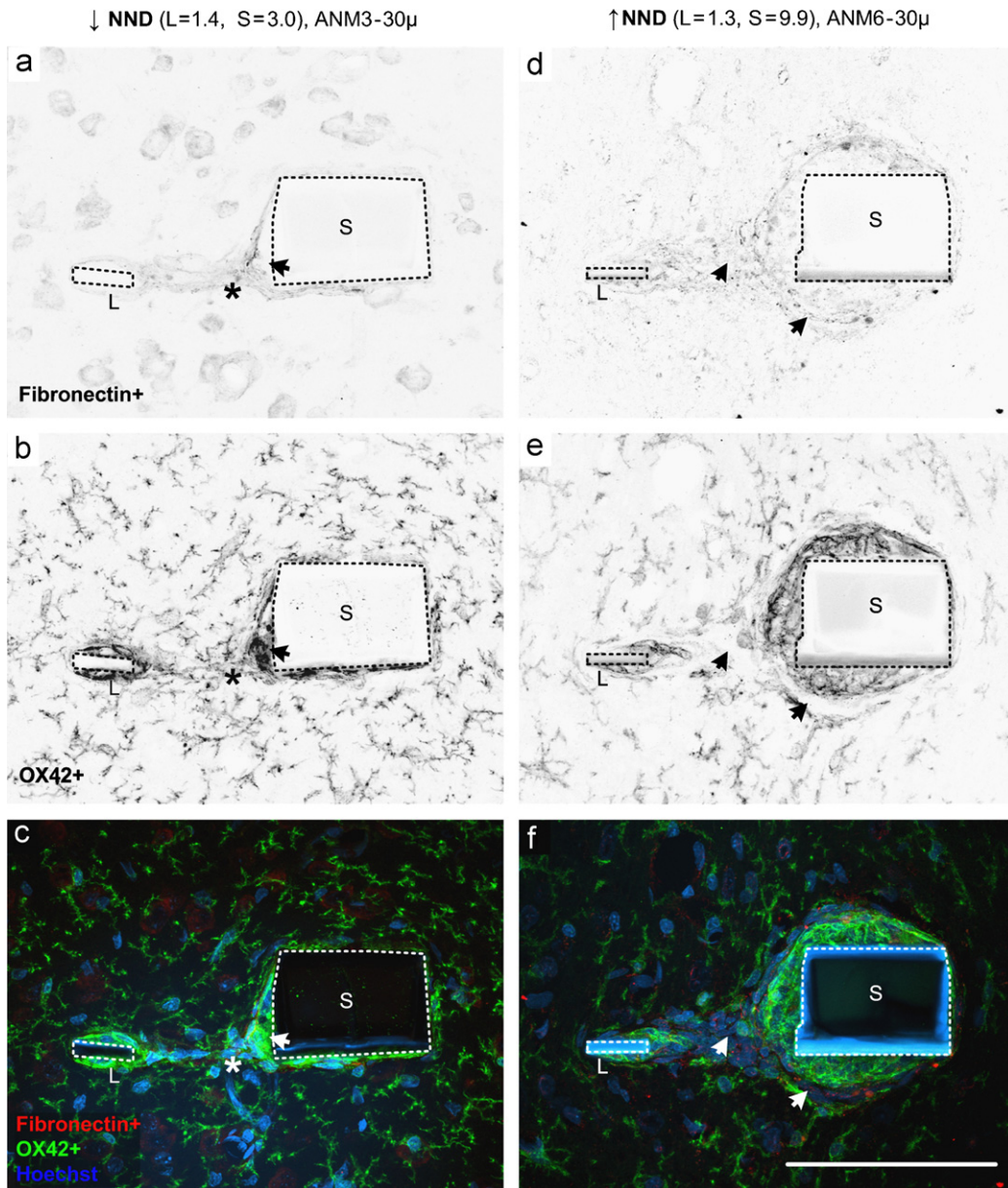


Fig. 9. Inverted grayscale IHC images (a, b, d, e) showing fibronectin (a, d) and OX-42 reactivity (b, e), and the corresponding RGB color image including Hoechst (c, f). Fibronectin staining had a pattern similar to laminin (Supplementary Fig. 1). (a–c) The low NND response had only a thin band of intensely labeled cells surrounded by ramified microglia just several microns distant. The inside corner of shanks (all probe types) usually exhibited intense OX-42 staining (b, e). (d–f) Fibronectin deposition extended 5–15 μm from the shank interface and was located with densely packed nuclei. While OX-42+ and fibronectin+ tissue were often concordant (* in a–c), highly encapsulated interfaces have nonoverlapping regions suggesting that not all cells were microglia (arrows, a–f). Scale = 100 μm. 60 × Obj.

probes [10,17]. Edell et al. reported significant loss (90% confidence level) in two rabbits out to 10 and 60 μm from the interface of silicon shanks (cross-section 40 × 60 μm). Using a slightly different metric, Biran et al. [10] reported a loss of 40% around a silicon probe in a 100-μm radius from the interface at both 2 and 4 weeks (cross-section 15 × 150 μm). When we averaged across all probes ($N = 28$) for a 75-μm radius, the shank region had a loss of 17%, and in the lateral region the loss was only 12% (calculated from Fig. 6 and weighted by area). There was no significant loss beyond the first 25 μm for any probe

type relative to the contralateral tissue. A number of differences between studies may account for our improved interface—we used a stereotaxic frame for insertion, intraparenchymal probes, and a different substrate material. Nonetheless, we are encouraged by the comparatively healthy interface around the shank of parylene probes, and that despite this we found significant advantage at the lateral edge. A direct comparison of encapsulation density is not possible since prior studies have not quantified this effect, but the variability and extent of encapsulation seems comparable [5,10,12,40].

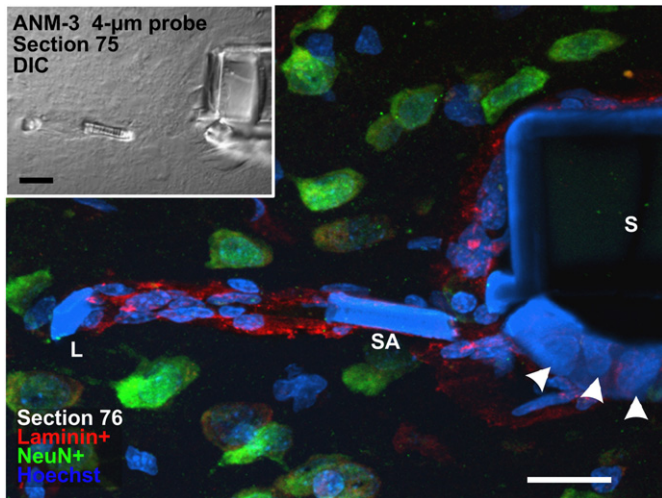


Fig. 10. Reactivity around the support arm of a 4- μm lattice platform. Two consecutive sections are shown, a DIC and IHC color image. Given a slight offset in the transverse sectioning angle, only a portion of the support arm (SA) was embedded in each. The tight but intense laminin staining in section 76 formed an outline of the support arm. Contrastingly, a single nucleus at the outside lateral edge was more spherical in shape. Cells on the surface of the probe shank conformed to the flat surface in a disc-like pattern (arrows). Shapes were evaluated using three-dimensional confocal images (not shown). Scale = 20 μm .

These results support our first hypothesis—that the far lateral region on a 5- μm -thick structure would have less encapsulation and neuronal loss because the reactive cells are presented with a narrow edge preventing the prototypical attachment and spreading seen in the foreign body response. More specifically, below a certain dimension a cell may not be able to attach and create tension in the cytoskeleton, which in turn disrupts the mechanotransduction pathway that may induce the unfavorable response [32,34,35]. In addition to the quantitative evidence, we believe the altered morphology seen around the various probe regions (Figs. 7, 9 and 10) supports this theory. Along the shank the nuclei were disc-like and spread out on the face of the probe (Fig. 10). At the lateral edge, there were rarely nuclei immediately present and nearby nuclei had smaller, spherical forms. However, our interpretation of these results is qualified by several possible confounding factors, namely flexibility, surface properties, and the influence of the lattice structure. The lateral edge not only presents a narrow feature, but also an increased flexibility relative to the probe shank. Surface properties on all outside or inside faces of the probe have a rough finish due to the reactive plasma etch used to define them. Since the shank and the inside lattice faces also had similar properties, this factor is of small concern. The influence of the lattice structure was controlled for by the 100- μm solid design, which was not significantly different. Future studies are needed to verify the mechanism causing the improvement at the lateral edge.

Our hypothesis regarding the tissue reactivity around a lattice structure expected the smallest lattice size (4 \times 5 μm) would induce the least encapsulation. Comparison between

probe designs indicated differences in encapsulation and neuronal loss was insignificant. Also, the qualitative histology inside the lattice region usually had a similar response as found around the shank. Thus, we believe our hypothesis about the lattice size is incorrect in this application. While both hypotheses were founded on the same principal of a mitigation of mechanotransduction, the tissue reactivity inside the lattice region has several confounding factors. First we point out that the differences in lattice width also affected the flexibility and surface properties. Most importantly, however, we believe a lattice structure presents a very different mechanical interface than a solid structure (i.e., shank). The brain is continually pulsating due to vascular and respiratory oscillations, and so small relative movement (micromotion) between a probe and tissue induces some level of strain [41–43]. Recently it was reported that the pial surface in the rat oscillates by as much as 30 μm during respiration [43]. This evidence of micromotion suggests that compressive forces and not just shear forces are at play within the lattice regions. Also, stress may be localized at inside edges and corners. The support arms and lateral edge were identical in size, but a consistent difference in reactivity was evident (Figs. 7–10), so more than size was influencing local reactivity. In brief, any benefits of the lattice and its small features could have been counterbalanced by the mechanical stresses due to micromotion. For future studies, longitudinal rather than transverse sections would provide improved visualization of the lattice structure and the resulting reactivity.

Despite considerable tissue reactivity inside the lattice region, several advantages may exist for an open-architecture design. The open-architecture may (1) provide improved tissue integration, (2) improve diffusion in local tissue, and (3) re-establish communication between either neurons or astrocytes that were initially severed during insertion. Liu et al. [4,22] reported that neuronal stability increases with time post-implant and is believed to be the result of tissue encapsulation anchoring the probes in place. It is reasonable to suggest that a lattice design will quicken the stabilization process (normally 2–3 months), which is an important factor in brain-machine applications. Normal forces inside the lattice structure should reduce probe migration. Re-establishing more neuronal and astrocytic (Ca^{2+} gap junctions) communication after injury both around and through the probe may be important for maintaining functional neurons. The lattice design would, in theory, enable more cell–cell contact. These last two effects would ideally mitigate the loss in nearby neuronal activity that has been hypothesized to reduce electrode function [44]. Further research is needed to characterize the mechanical and cellular interactions in and around a lattice structure especially when tethering is used, but this design concept is promising.

The double label immunostaining revealed two different types of glial reactivity. The first and more benevolent was a thin boundary of activated microglia at the interface intermingled with hypertrophied astrocytic processes.

Unlike activated microglia, the hypertrophied astrocytes usually coexisted with neurons. This first type characterized the tissue about the lateral edge and only occasionally the region about the shank. The second type of reactive tissue was a noticeably thicker capsular region devoid of GFAP, neurofilament, and NeuN but always OX-42 positive and often fibronectin and laminin positive as well. Here the neuronal loss and nonneuronal encapsulation is most evident. However, the variability at the lateral edge of these probes was far less. The tissue around the lateral edge was consistently GFAP positive, and usually laminin negative and fibronectin negative. Further, microglia and other nonneuronal cells did not conform to the edge of the structure and thus may contribute less to the electrical impedance between this point on the probe and a distant neuron.

One theory that could explain the two types of glial tissue around the shank of the probe is the presence or lack of meningeal cells. Meningeal cells have been reported to play an active role in stab wound injuries and form an “accessory glia limitans” [13,16,39,45]. Some have suggested their presence around neural probes [14,26]. The presence of fibronectin+/OX-42– tissue suggests that some of the nonneuronal nuclei may be fibroblasts of meningeal origin. Their presence would explain why astrocytes seemingly circumscribe the tissue several to tens of microns from the shank, and why some tissue is fibronectin+ but not OX-42+ (Fig. 9). This is important because the existence of fibroblasts and the resulting astrocyte–meningeal interface may further increase the impedance between the electrode and spiking neurons [44].

Regarding the fabrication of these structures, we chose a substrate of poly-para-xylylene (specifically parylene-C) for

several reasons: (1) microfabrication techniques are well established, (2) Class VI USP biocompatibility rating, (3) excellent insulating properties [46], (4) low water uptake of 0.06%, (5) elongation at break is 200% [47], and (6) a polymer probe can be left in situ to improve the spatial resolution of the histological analysis. While the probe surface is parylene, the core of the shank consists of SU-8, an epoxy based photoresist that has been well characterized. This material can achieve thick layers in one application whereas parylene is typically deposited less than 10 μm each run. SU-8 is also reported to be noncytotoxic [48,49]. However, other noncytotoxic materials such as silicon dioxide, silicon, and polyimide to name a few, would be expected to confer the same results if designed with similar dimensions.

The pattern of cellular encapsulation and neuronal loss suggests an electrode site design that wraps-around the perimeter. To effectively use the limited substrate at the perimeter around a neural probe or biosensor in the CNS, the electrode surface should be on three sides of the probe (Fig. 11, data taken from Fig. 6(b)). This would also maximize surface area facing healthy tissue. Another benefit of such a design would be an increase in the sensor viewing radius from 180° to almost 360° because there is less shielding [50]. However, there are two possible difficulties: (1) the fabrication complexity of creating a three dimensional electrode on a planar substrate, and (2) the size and surface limitation imposed may reduce sensitivity. In the case of a neural probe, we believe these are attainable engineering goals. Regarding the former concern, one may use electroplating to create a thick electrode, which is commonly done with contact vias in integrated and printed circuits. To address the latter, the

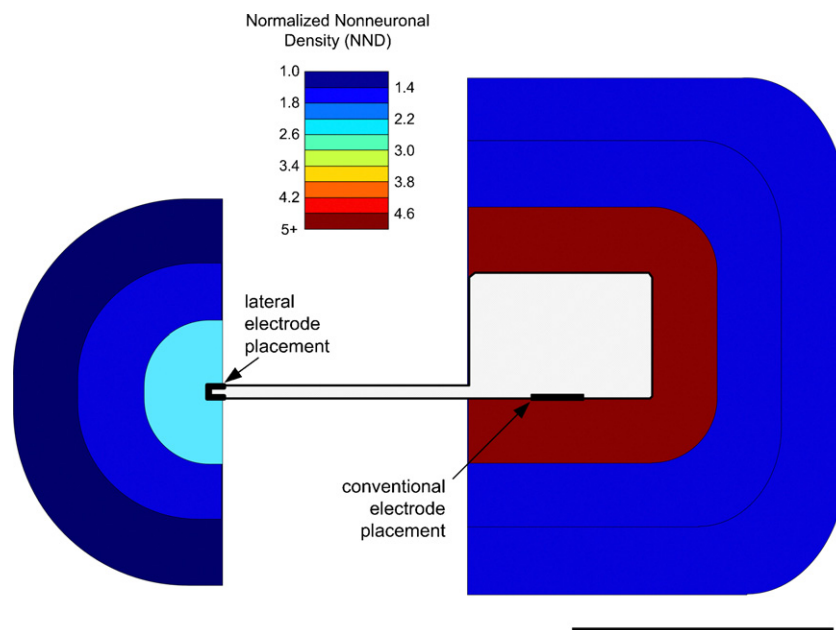


Fig. 11. A graphical illustration of the importance of electrode placement. The graph shows the regions of tissue and the corresponding average nonneuronal density for all probe types (data taken from Fig. 5(b)). Regardless of probe type, the histological results indicated that the best electrode placement would be at the lateral edge. All probes tested had an identical footprint, as seen in a transverse cross-section. Scale = 100 μm .

effective surface area can be greatly increased with the use of platinum black [51], oxidized iridium [52], or conductive polymers. In some applications, such as recording spike activity, sensitivity is expected to increase with decreased surface area.

5. Conclusions

Quantification of high-resolution confocal images around intact probe structures revealed that encapsulating cell density within 25 μm of a thin lateral structure is reduced by almost one-third relative to the shank. The difference in neuronal loss was also significant. Furthermore, activated microglia and protein deposition is greatly reduced at this surface. Also, this study proves these probes are mechanically robust and practical as neural probes, despite utilizing a polymer substrate with subcellular dimensions.

We conclude that the ideal electrode placement for the tested probe designs is on the outermost edge of a 5- μm -thick platform extending far from the probe shank. These results suggest it would be worthwhile to implement this alternative neural probe design in the CNS. Investigating the effect of subcellular dimensions and electrode placement in other biosensor designs should also be considered.

Acknowledgements

The authors acknowledge Dr. David Pellinen for fabrication advice and training and Dr. William Shain for reviewing the manuscript. The authors also thank Dr. Jeyakumar Subbaroyan, Erin Purcell, Kip Ludwig and other members of the Neural Engineering Laboratory and the Center for Neural Communication Technology for technical assistance and discussion. The staff at the Michigan Nanofabrication Facility and the Microscopy and Imaging Laboratory provided excellent support. Funding for this research was provided in part by the National Institute for Biomedical Imaging and Bioengineering (NIBIB) Grant P41 EB002030, the Engineering Research Centers program of the National Science Foundation under NSF Award no. EEC-9986866, and the Department of Defense Multidisciplinary University Research Initiative (MURI) grant no. W911NF0610218.

Appendix A. Supplementary data

Supplementary data associated with this article can be found in the online version at [doi:10.1016/j.biomaterials.2007.03.024](https://doi.org/10.1016/j.biomaterials.2007.03.024).

References

[1] Buzsaki G. Large-scale recording of neuronal ensembles. *Nature Neurosci* 2004;7(5):446–51.

[2] Hochberg LR, Serruya MD, Friehs GM, Mukand JA, Saleh M, Caplan AH, et al. Neuronal ensemble control of prosthetic devices by a human with tetraplegia. *Nature* 2006;442(7099):164–71.

[3] Schwartz AB. Cortical neural prosthetics. *Annu Rev Neurosci* 2004;27:487–507.

[4] Liu X, McCreery DB, Bullara LA, Agnew WF. Evaluation of the stability of intracortical microelectrode arrays. *IEEE Trans Neural Syst Rehab Eng* 2006;14(1):91–100.

[5] Rousche PJ, Normann RA. Chronic recording capability of the Utah intracortical electrode array in cat sensory cortex. *J Neurosci Methods* 1998;82(1):1–15.

[6] Santucci DM, Kralik JD, Lebedev MA, Nicolelis MA. Frontal and parietal cortical ensembles predict single-trial muscle activity during reaching movements in primates. *Eur J Neurosci* 2005;22(6):1529–40.

[7] Suner S, Fellows MR, Vargas-Irwin C, Nakata GK, Donoghue JP. Reliability of signals from a chronically implanted, silicon-based electrode array in non-human primate primary motor cortex. *IEEE Trans Neural Syst Rehab Eng* 2005;13(4):524–41.

[8] Vetter RJ, Williams JC, Hetke JF, Nunamaker EA, Kipke DR. Chronic neural recording using silicon-substrate microelectrode arrays implanted in cerebral cortex. *IEEE Trans Biomed Eng* 2004;51(6):896–904.

[9] Williams JC, Rennaker RL, Kipke DR. Long-term neural recording characteristics of wire microelectrode arrays implanted in cerebral cortex. *Brain Res Brain Res Protoc* 1999;4(3):303–13.

[10] Biran R, Martin DC, Tresco PA. Neuronal cell loss accompanies the brain tissue response to chronically implanted silicon microelectrode arrays. *Exp Neurol* 2005;195(1):115–26.

[11] Maynard EM, Fernandez E, Normann RA. A technique to prevent dural adhesions to chronically implanted microelectrode arrays. *J Neurosci Methods* 2000;97(2):93–101.

[12] Szarowski DH, Andersen MD, Retterer S, Spence AJ, Isaacson M, Craighead HG, et al. Brain responses to micro-machined silicon devices. *Brain Res* 2003;983(1–2):23–35.

[13] Shearer MC, Fawcett JW. The astrocyte/meningeal cell interface—a barrier to successful nerve regeneration? *Cell Tissue Res* 2001;305(2):267–73.

[14] Kim YT, Hitchcock RW, Bridge MJ, Tresco PA. Chronic response of adult rat brain tissue to implants anchored to the skull. *Biomaterials* 2004;25(12):2229–37.

[15] Hampton DW, Rhodes KE, Zhao C, Franklin RJ, Fawcett JW. The responses of oligodendrocyte precursor cells, astrocytes and microglia to a cortical stab injury, in the brain. *Neuroscience* 2004;127(4):813–20.

[16] Fawcett JW, Asher RA. The glial scar and central nervous system repair. *Brain Res Bull* 1999;49(6):377–91.

[17] Edell DJ, Toi VV, McNeil VM, Clark LD. Factors influencing the biocompatibility of insertable silicon microshafts in cerebral cortex. *IEEE Trans Biomed Eng* 1992;39(6):635–43.

[18] Roitbak T, Sykova E. Diffusion barriers evoked in the rat cortex by reactive astrogliosis. *Glia* 1999;28(1):40–8.

[19] Johnson MD, Otto KJ, Kipke DR. Repeated voltage biasing improves unit recordings by reducing resistive tissue impedances. *IEEE Trans Neural Syst Rehab Eng* 2005;13(2):160–5.

[20] Ludwig KA, Uram JD, Yang J, Martin DC, Kipke DR. Chronic neural recordings using silicon microelectrode arrays electrochemically deposited with a poly(3,4-ethylenedioxythiophene) (PEDOT) film. *J Neural Eng* 2006;3(1):59–70.

[21] Nicholson C, Sykova E. Extracellular space structure revealed by diffusion analysis. *Trends Neurosci* 1998;21(5):207–15.

[22] Liu X, McCreery DB, Carter RR, Bullara LA, Yuen TG, Agnew WF. Stability of the interface between neural tissue and chronically implanted intracortical microelectrodes. *IEEE Trans Rehab Eng* 1999;7(3):315–26.

[23] Schmidt EM, McIntosh JS, Bak MJ. Long-term implants of Parylene-C coated microelectrodes. *Med Biol Eng Comput* 1988;26(1):96–101.

- [24] McCreery DB, Agnew WF, McHardy J. Electrical characteristics of chronically implanted platinum-iridium electrodes. *IEEE Trans Biomed Eng* 1987;34(9):664–8.
- [25] Lefurge T, Goodall E, Horch K, Stensaas L, Schoenberg A. Chronically implanted intrafascicular recording electrodes. *Ann Biomed Eng* 1991;19(2):197–207.
- [26] Cui X, Lee VA, Raphael Y, Wiler JA, Hetke JF, Anderson DJ, et al. Surface modification of neural recording electrodes with conducting polymer/biomolecule blends. *J Biomed Mater Res* 2001;56(2):261–72.
- [27] He W, Bellamkonda RV. Nanoscale neuro-integrative coatings for neural implants. *Biomaterials* 2005;26(16):2983–90.
- [28] Zhong Y, Bellamkonda RV. Controlled release of anti-inflammatory agent alpha-MSH from neural implants. *J Control Release* 2005;106(3):309–18.
- [29] Kim DH, Martin DC. Sustained release of dexamethasone from hydrophilic matrices using PLGA nanoparticles for neural drug delivery. *Biomaterials* 2006;27(15):3031–7.
- [30] Shain W, Spataro L, Dilgen J, Haverstick K, Retterer S, Isaacson M, et al. Controlling cellular reactive responses around neural prosthetic devices using peripheral and local intervention strategies. *IEEE Trans Neural Syst Rehab Eng* 2003;11(2):186–8.
- [31] Bernatchez SF, Parks PJ, Gibbons DF. Interaction of macrophages with fibrous materials in vitro. *Biomaterials* 1996;17(21):2077–86.
- [32] Sanders JE, Stiles CE, Hayes CL. Tissue response to single-polymer fibers of varying diameters: evaluation of fibrous encapsulation and macrophage density. *J Biomed Mater Res* 2000;52(1):231–7.
- [33] Turner AM, Dowell N, Turner SW, Kam L, Isaacson M, Turner JN, et al. Attachment of astroglial cells to microfabricated pillar arrays of different geometries. *J Biomed Mater Res* 2000;51(3):430–41.
- [34] Chen CS, Tan J, Tien J. Mechanotransduction at cell–matrix and cell–cell contacts. *Annu Rev Biomed Eng* 2004;6:275–302.
- [35] Chen CS, Mrksich M, Huang S, Whitesides GM, Ingber DE. Geometric control of cell life and death. *Science* 1997;276(5317):1425–8.
- [36] Rousche PJ, Normann RA. A method for pneumatically inserting an array of penetrating electrodes into cortical tissue. *Ann Biomed Eng* 1992;20(4):413–22.
- [37] Bjornsson CS, Oh SJ, Al-Kofahi YA, Lim YJ, Smith KL, Turner JN, et al. Effects of insertion conditions on tissue strain and vascular damage during neuroprosthetic device insertion. *J Neural Eng* 2006;3(10):196–207.
- [38] Schwartz M, Butovsky O, Bruck W, Hanisch UK. Microglial phenotype: is the commitment reversible? *Trends Neurosci* 2006;29(2):68–74.
- [39] Bundesen LQ, Scheel TA, Bregman BS, Kromer LF. Ephrin-B2 and EphB2 regulation of astrocyte-meningeal fibroblast interactions in response to spinal cord lesions in adult rats. *J Neurosci* 2003;23(21):7789–800.
- [40] Turner JN, Shain W, Szarowski DH, Andersen M, Martins S, Isaacson M, et al. Cerebral astrocyte response to micromachined silicon implants. *Exp Neurol* 1999;156(1):33–49.
- [41] Goldstein SR, Salcman M. Mechanical factors in the design of chronic recording intracortical microelectrodes. *IEEE Trans Biomed Eng* 1973;20(4):260–9.
- [42] Subbaroyan J, Martin DC, Kipke DR. A finite-element model of the mechanical effects of implantable microelectrodes in the cerebral cortex. *J Neural Eng* 2005;2(4):103–13.
- [43] Gilletti A, Mushuswamy J. Brain micromotion around implants in the somatosensory cortex of rats. *J Neural Eng* 2006;3:189–95.
- [44] Merrill DR, Tresco PA. Impedance characterization of microarray recording electrodes in vitro. *IEEE Trans Biomed Eng* 2005;52(11):1960–5.
- [45] Shearer MC, Niclou SP, Brown D, Asher RA, Holtmaat AJ, Levine JM, et al. The astrocyte/meningeal cell interface is a barrier to neurite outgrowth which can be overcome by manipulation of inhibitory molecules or axonal signalling pathways. *Mol Cell Neurosci* 2003;24(4):913–25.
- [46] Loeb GE, Peck RA, Martyniuk J. Toward the ultimate metal microelectrode. *J Neurosci Methods* 1995;63(1–2):175–83.
- [47] Fortin JB, Lu TM. Chemical vapor deposition polymerization: the growth and properties of parylene thin films. Boston: Kluwer Academic Publishers; 2004.
- [48] Kotzar G, Freas M, Abel P, Fleischman A, Roy S, Zorman C, et al. Evaluation of MEMS materials of construction for implantable medical devices. *Biomaterials* 2002;23(13):2737–50.
- [49] Voskerician G, Shive MS, Shawgo RS, von Recum H, Anderson JM, Cima MJ, et al. Biocompatibility and biofouling of MEMS drug delivery devices. *Biomaterials* 2003;24(11):1959–67.
- [50] Moffitt MA, McIntyre CC. Model-based analysis of cortical recording with silicon microelectrodes. *Clin Neurophysiol* 2005;116(9):2240–50.
- [51] Ilic B, Czaplinski D, Neuzil P, Stanczyk T, Blough J, Maclay GJ. Preparation and characterization of platinum black electrodes. *J Mater Sci* 2000;35(14):3447–57.
- [52] Lee I-S, Whang C-N, Choi K, Choo M-S, Lee Y-H. Characterization of iridium film as a stimulating neural electrode. *Biomaterials* 2002;23(11):2375–80.